Article

Recycling Silicon Waste from Photovoltaic Industry to Prepare Yolk-Shell Si@void@C Anode Materials for Lithium-Ion Batteries

Hengsong Ji[1], Zhijin Liu[1], Xiang Li[2,3*], Jun Li[1], Zexuan Yan[2] and Kai Tang[4*]

1 Institute of Energy Research, Jiangsu University, Zhenjiang 212013, China;
2 School of Energy and Power Engineering, Jiangsu University, Zhenjiang 212013, China;
3 Taizhou DongBo New Materials Co. Ltd., Taizhou, 225312, China
4 SINTEF Industry, N-7465 Trondheim, Norway
* Correspondence: xiangli@ujs.edu.cn (X.L.); kai.tang@sintef.no (K.T.)

Abstract: Silicon has a theoretical specific capacity of 4200 mAh g^{-1}, which is considered to have significant potential for anode materials in lithium-ion batteries (LIBs). However, the volume change that occurs in silicon during charging and discharging affects the development of commercial applications. In this work, a yolk-shell structured Si@void@C anode material has been developed to address this problem. The silicon nanoparticle yolk material is obtained by recycling kerf-loss (KL) Si waste from the photovoltaic industry, the carbon shell is prepared via a hydrothermal process with glucose, and the sacrificial interlayer is Al_2O_3. The synthesized material is used to fabricate anodes that show a high reversible capacity of 836 mAh g^{-1} at the current density of 0.1 A g^{-1} after 100 cycles, with a Coulomb efficiency of 71.4%. This work demonstrates a relatively low-cost approach to turn KL Si waste into value-added materials for LIBs.

Keywords: Lithium-ion batteries; Anode; Kerf-loss Si waste; Yolk-shell structure

1. Introduction

Lithium-ion batteries (LIBs) have become the most widely used energy storage devices because of their high energy density and rate performance [1-4]. However, commercialized LIBs are mostly based on graphite anodes and cannot meet the increasing demand for greater energy density [5-8]. Therefore, the development of improved cathode materials for LIBs is required. The theoretical specific capacity of Si is 4500 mAh g^{-1}, which is more than 10 times the theoretical specific capacity of the carbon electrodes currently used in LIBs [9-12]. Moreover, it is estimated that more than 2.6×10^5 tons of kerf-loss (KL) Si waste are discarded every year [13-16]. Notably, using KL Si waste as an anode material in LIBs not only reduces the production cost of Si-based anode but also reduces waste and excessive hoarding. Such resources can generate significant commercial value if used properly. However, in the process of charging and discharging, Si undergoes substantial volumetric expansion (~300%), which leads to the fracture of Si particles, and eventually, the active material breaks off from the collector, deteriorating the electrochemical performance [17-20].

Many researchers have made contributions attempting to solve this problem. Yang [21] used HF and NaOH to etch KL Si waste. The Si etched by HF exhibited a porous structure, and sodium hydroxide etching produced a sheet structure. At the current density of 0.42 A g^{-1}, the discharge-specific capacity of 600.7 mAh g^{-1} was obtained after 200 cycles. Liu [22] proposed a simple coprecipitation method of Si and lignin using electrostatic attraction, followed by a thermal annealing process, to produce a high-capacity Si/C cathode material. This composite material showed a charging capacity of 1016.8 mAh g^{-1} at a current density of 0.2 A g^{-1}, and its capacity retention rate was 74.5% after 100 cycles. Zhang [23] used KL Si waste to synthesize silver nanoparticles under DC thermal plasma conditions and then combined them with Si to obtain Si@SiO_x@Ag nanocomposite anode materials. The material exhibited a high initial Coulombic efficiency of 89.9% and a large initial

Preprints (www.preprints.org) | NOT PEER-REVIEWED | Posted: 12 May 2023 doi:10.20944/preprints202305.0901.v1

discharge capacity of 2919 mAh g^{-1} at 0.5 A g^{-1}. Even after 200 charge-discharge cycles, the reversible capacity exceeded 1000 mAh g^{-1}. Overall, the basic treatment methods for KL Si waste include carbon recombination, metal recombination, and structural improvement, which have been employed to mitigate the large volumetric change of Si during charging and discharging.

In this paper, diamond-wire-cut multicrystalline Si waste is selected as Si source, glucose is used as the carbon source, the intermediate sacrificial layer is prepared by metathesis reaction, the carbon layer is formed by hydrothermal reaction, and the yolk-shell structure is formed by etching. The structure consists of Si nanoparticles as the core and graphite carbon as the outer yolk-shell structure. The hollow structure in the shell can effectively alleviate the volumetric expansion effect of Si particles. This material design strategy for the production of LIBs anodes of high capacity and cycle stability turns KL Si waste into value-added materials.

2. Materials and Methods

2.1. Pretreatment of KL Si waste

The KL multicrystalline Si waste was supplied by Jinko Power Technology Co., Ltd from diamond-wire sawing (DWS) process. It was cleaned with anhydrous ethanol 3 times and subsequently calcined for 1 h at 800 °C in an Ar atmosphere to remove the organic impurities. Then, the powder was pickled with 10 wt% hydrochloric acid for 30 min and then cleaned with deionized water 3 times to remove trace metal ions in the powder. After centrifugation, the powder was dried in an Ar atmosphere at 50 ℃ to obtain microscale Si powder. Then, nanoscale Si powder (200–500 nm) was obtained after wet grinding at 600 rpm for 4 h, followed by centrifugal drying. Agate beads with diameters of 3.5 mm and 1.0 mm were used as the abrasive grinding material, and the weight ratio of beads to Si powder was 20:1.

2.2. Synthesis of Si@void@C

Figure 1 illustrates the formation process of yolk-shell Si@void@C composite. Firstly, a certain amount of $AlCl_3$ were weighted and dissolved into 10 mL of deionized water in a beaker. Then, 10 ml of ammonia and 0.4 g of pretreated Si powder were added into the solution. After magnetic stirring with ultrasonication for 2 h, the mixture were collected by centrifugal drying. The dired mixture were calcined at 700 ℃ for 2 h with a horizontal tube furnace in an Ar atmosphere. Samples with $AlCl_3$/Si weight ratio of 2:1, 1:1, and 1:2 were named as SA-21, SA-11, and SA-12, respectively.

Secondly, 0.4 g of SA-21, SA-11, or SA-12 was weighted into a beaker containing 25 mL of deionized water. Then, 1.2 g of glucose monohydrate was added to the above solution, followed by magnetic stirring with ultrasonication for 30 min. The resulting precipitate was transferred into a Teflflon-lined stainless autoclave, which was kept at 180 °C for 8 h. After that the resulting product was washed with deionized water and dried at 80 °C, and calcined at 800 ℃ for 2 h in an Ar atmosphere. The obtained samples were named as SAC-21, SAC-11, and SAC-12, respectively.

Finally, SAC samples were pickled with 4 mol/L hydrochloric acid solution for 24 h and then cleaned with deionized water 3 times. The obtained samples were named as SVC-21, SVC-11, and SVC-12, respectively.

Preprints (www.preprints.org) | NOT PEER-REVIEWED | Posted: 12 May 2023 doi:10.20944/preprints202305.0901.v1

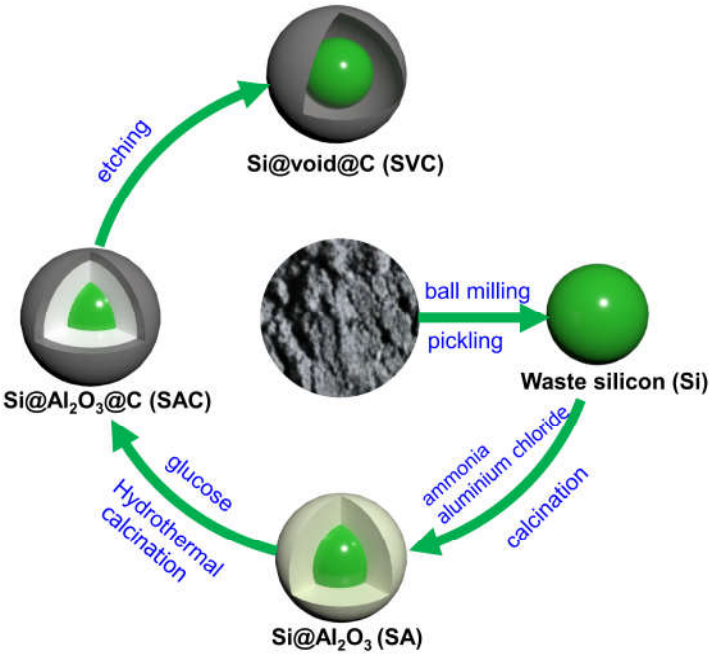

Figure 1. Illustration of the Si@void@C composite preparation.

2.3. Materials characterization

The morphologies of the samples were characterized by scanning electron microscopy (SEM, JEOL JSM-7800F, Tokyo, Japan) and transmission electron microscopy (TEM, FEI Talos F200x G2, USA), energy dispersive X-ray spectroscopy (EDS) were used to characterize the elemental distribution of samples. The crystalline structures of the products were examined using X-ray diffraction (XRD, Bruker D8, USA) with Cu Kα radiation. The surface composition of the sample was investigated using X-ray photoelectron spectroscopy (XPS, Thermo Fisher K-Alpha Nexsa, USA). Raman system (DXR, Thermo Fisher, USA) with a 532 nm laser was used to prove the existence of Si and C and examine the structure of carbon.

2.4. Electrochemical Measurements

The electrochemical performance of Si@void@C material was evaluated by using CR2032 coin-type half cells with lithium foil as counter and reference electrodes. The active material, the carbon black conductive agent, and the polyvinylidene fluoride binder were mixed and dissolved in N-methylpyrrolidone at a ratio of 8:1:1. The slurry was coated on the carbon-coated copper foil, followed by vacuum drying at 100 °C for 12 h. The mass loading of electrodes is about 1.0 mg cm^{-2}. Subsequently, the tested half cells were assembled in an Ar-filled glove box. Celgard 2400 was used as the separator, with the mixture of 1.2 M $LiPF_6$+EC/DEC/EMC(1:1:1) +10% FEC as the electrolyte.

Cyclic voltammetry (CV) at various scanning rates, galvanostatic charge-discharge (GCD) measurements at various current densities, and electrochemical impedance spectroscopy (EIS) measurements in the frequency from 100 kHz to 0.01 Hz were performed on an Ivium-n-Start Electrochemical Workstation. Charge/discharge tests were performed on a Neware BTS-5V10mA battery test system under different current densities between 0.01-1.2 V.

3. Results

3.1. Material Morphology, Structure, and Chemical Composition

The SEM images of SVC-21, SVC-11, and SVC-12 are shown in Figure 2a, b and c, respectively. All the three samples contain sheet-like structures mixed with uneven spheres. The spherical structures are due to the decomposition of glucose into soluble molecules such as aromatic

Preprints (www.preprints.org) | NOT PEER-REVIEWED | Posted: 12 May 2023 doi:10.20944/preprints202305.0901.v1

compounds, organic acids, and oligosaccharides in the hydrothermal reaction. After polymerization and aromatization, these molecules will diffuse around with a particle as the core to grow carbon spheres [24]. The addition of metal ions (Al^{3+}) in the hydrothermal process will accelerate the polymerization process and promote the formation of spherical structures [25]. EDS mapping result of SAC-21, SAC-11, and SAC-12, shown in Figure 3a, b and c respectively, indicates that the sheet-like structure mainly contains C and Si, and the spherical mainly contains C. The uniformly distributed Al and O indicate that a layer of Al_2O_3 was synthesized, which is also proved by the TEM image of SAC-11 shown in Figure 4.

Figure 2d, e, and f presents the TEM image of SVC-21, SVC-11, and SVC-12, respectively. In all samples, Si particls are wrapped with amorphous carbon shell with void space between the Si core and carbon shell, leading to a good dispersion and aggregation resistant of Si particls.

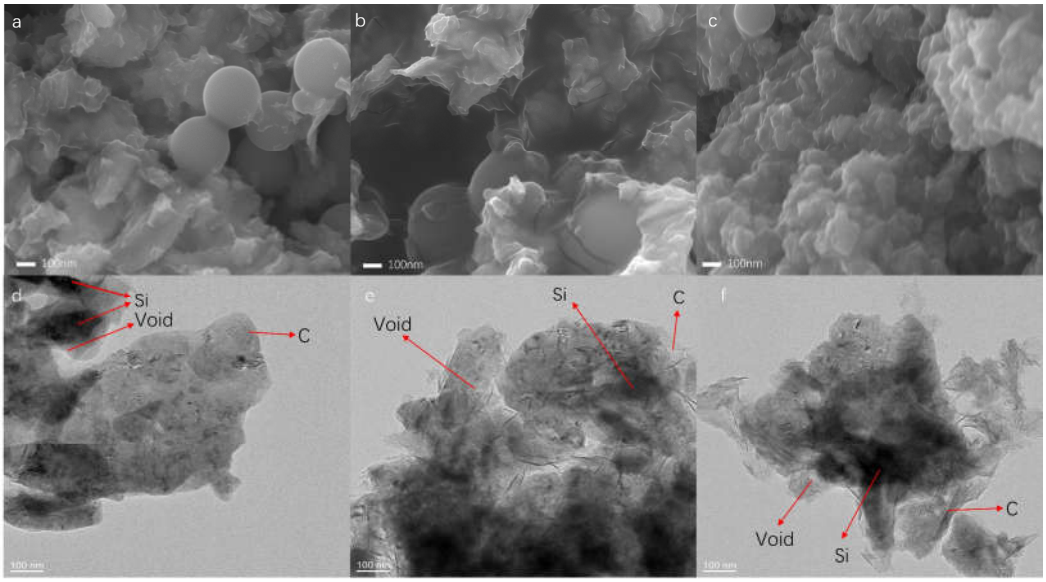

Figure 2. SEM image of (a) SVC-21, (b) SVC-11, (c) SVC-12. TEM image of (d) SVC-21, (e) SVC-11, (f) SVC-12.

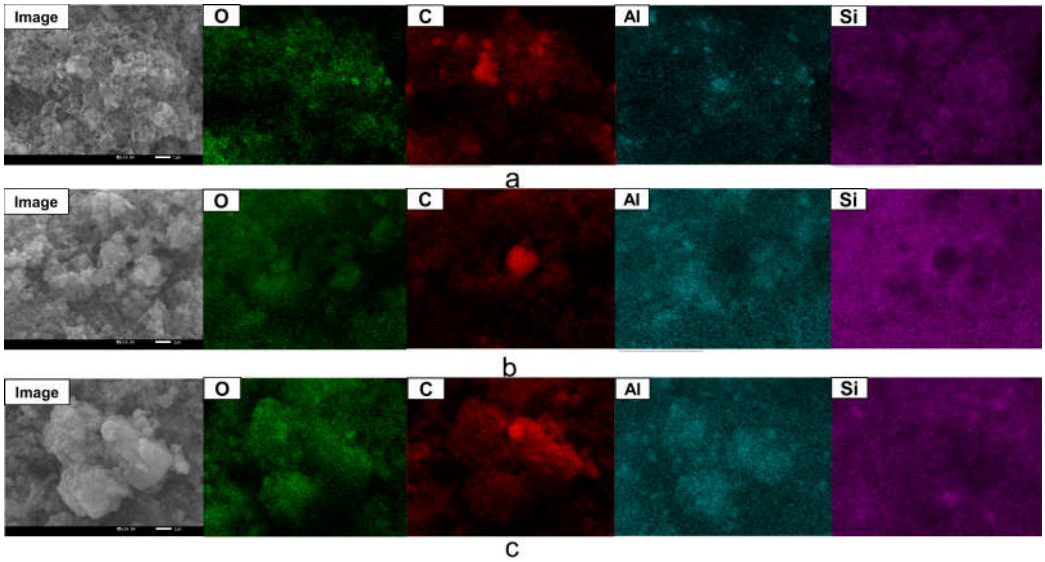

Figure 3. EDS mapping results of (a) SAC-21, (b) SAC-11, and (c) SAC-12.

Preprints (www.preprints.org) | NOT PEER-REVIEWED | Posted: 12 May 2023 doi:10.20944/preprints202305.0901.v1

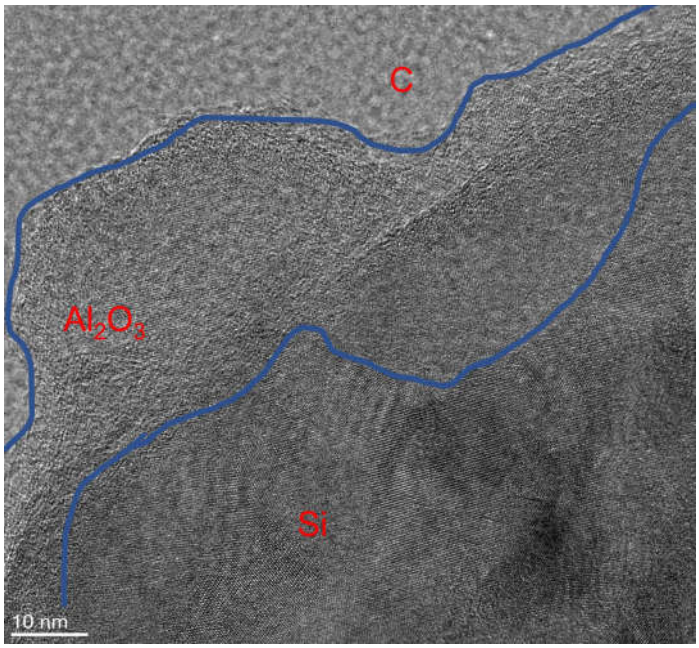

Figure 4. HRTEM image of SAC-11.

The XRD patterns of SAC and SVC samples are presented in Figure 5. SAC samples exhibit mixture phase of Si and Al_2O_3, which consistent with EDS mapping results shown in Figure 3. Of note is that Al_2O_3 peaks increased significantly with the increase of the $AlCl_3$/Si weight ratio during the stnthesis of SAC. In the patterns of SVC samples, Al_2O_3 phase disappears due to the acid pickling process. And C peaks were not detected as the C in SVC samples presents amorphous phase [26].

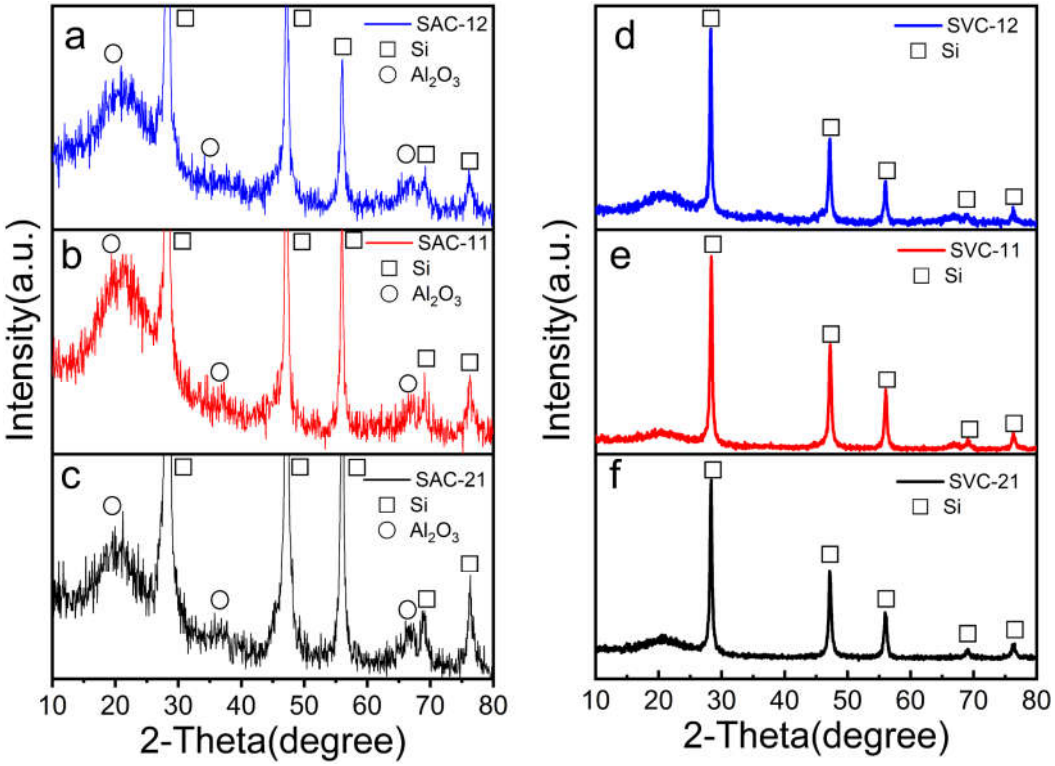

Figure 5. XRD of (a) SAC-12, (b) SAC-11, (c) SAC-21; (d) SVC-12, (e) SVC-11, and (f) SVC-21.

XPS was performed to examine the elemental composition of the SVC-11, as shown in Figure 6. The prominent peaks are associated with C 1s, Si 2p, Si 2s, O 1s and Al 2p (Figure 6a), indicating the presence of the Si, C, O and Al [27, 28], where Al is from the resistant Al_2O_3 after acid pickling of

Preprints (www.preprints.org) | NOT PEER-REVIEWED | Posted: 12 May 2023 doi:10.20944/preprints202305.0901.v1

SAC-11. The C 1s XPS spectra also reveals the binding confifigurations of oxygen and carbon in the SVC-11 (Figure 6b). The C1s XPS spectra is deconvoluted to three different peaks: C-C bond (284.8 eV), C-O bond (286.2 eV) and C=O bond (288.8 eV) [29]. The Si 2p XPS spectra of SVC-11 is shown in Figure 6c, which is deconvoluted to three different peaks: Si-Si bond (99.6eV), Si-C bond (100.2 eV) and Si-O bond (103.5 eV) [30]. Figure 6d presents the Raman spectra of SVC-11. In addition to the strong Si peak near 518 cm^{-1}, there are two characteristic peaks for carbon at 1350 and 1590 cm^{-1}. The former is associated with the amorphous carbon materials, while the latter is attributed to the vibration of sp^2-bonded in typical graphite [31, 32]. The I_D/I_G ratio of the SVC-11 is estimated to be 0.88, indicating a relatively high degree of graphitization, which is favourable to improve the electrical conductivity of the carbon shell [33].

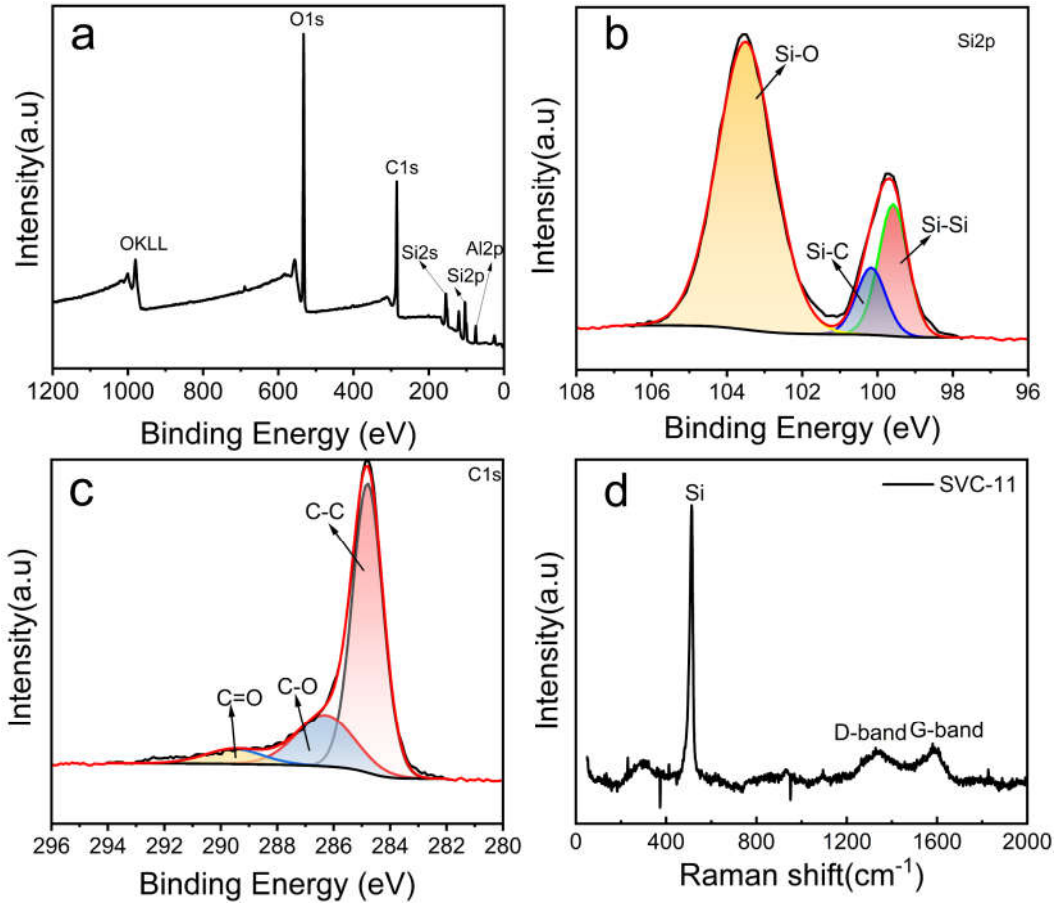

Figure 6. XPS survey of SVC-11 (a); high resolution of XPS pectra for (b) C 1s and (c) Si 2p; (d)Raman spectra of SVC-11.

3.2. Electrochemical Performance of Si@void@C

The electrochemical performance of Si@void@C samples were evaluated based on half-cell configurations. CV was performed with scanning speed of 0.1 mV s^{-1} at voltage of 0.01–1.1 V, as shown in Figure 7a, b, and c. The CV curves of all three samples are similar. In the first discharge, the broad reduction peak at around 0.7 V corresponds to the irreversible reaction between Li^+ ions and Si surface functional groups, as well as the solid electrolyte mesophase, which disappeared in subsequent cycles [34]. The other reduction peak observed around 0.20 V is attributed to the formation of Li_xSi, and the two oxidation peaks near 0.31 and 0.49 V are due to Li_xSi and Si dealloying [35, 36]. In the later cycles, the current values of the two oxidation peaks increase significantly, which is due to the activation of more Si atoms in the material. Importantly, the CV curves almost overlap after the second cycle, indicating that the anode material exhibits high reversibility.

EIS was performed to understand electrical conductivity and ion diffusion variations of the fresh electrode. The Nyquist plots of fresh SVC-21, SVC-11, and SVC-12 electrodes are presented in Figure 7d, e, and f, respectively. Only one semicircle in the high-frequency region is observed in all three

Preprints (www.preprints.org) | NOT PEER-REVIEWED | Posted: 12 May 2023 doi:10.20944/preprints202305.0901.v1

Nyquist plots, which corresponds to the charge transfer resistance (R_{ct}) between active materials and electrolyte interface. A straight line in the low-frequency region is observed, which corresponds to Warburg diffusion impedance [37]. The charge transfer resistance (R_{ct}) of SVC-21, SVC-11, and SVC-12 is 176, 65, and 87 Ω, respectively. The R_{ct} value of SVC-11 is obviously lower than that of SVC-21 and SVC-12, which indicates the enhanced charge transfer kinetics of SVC-11[38].

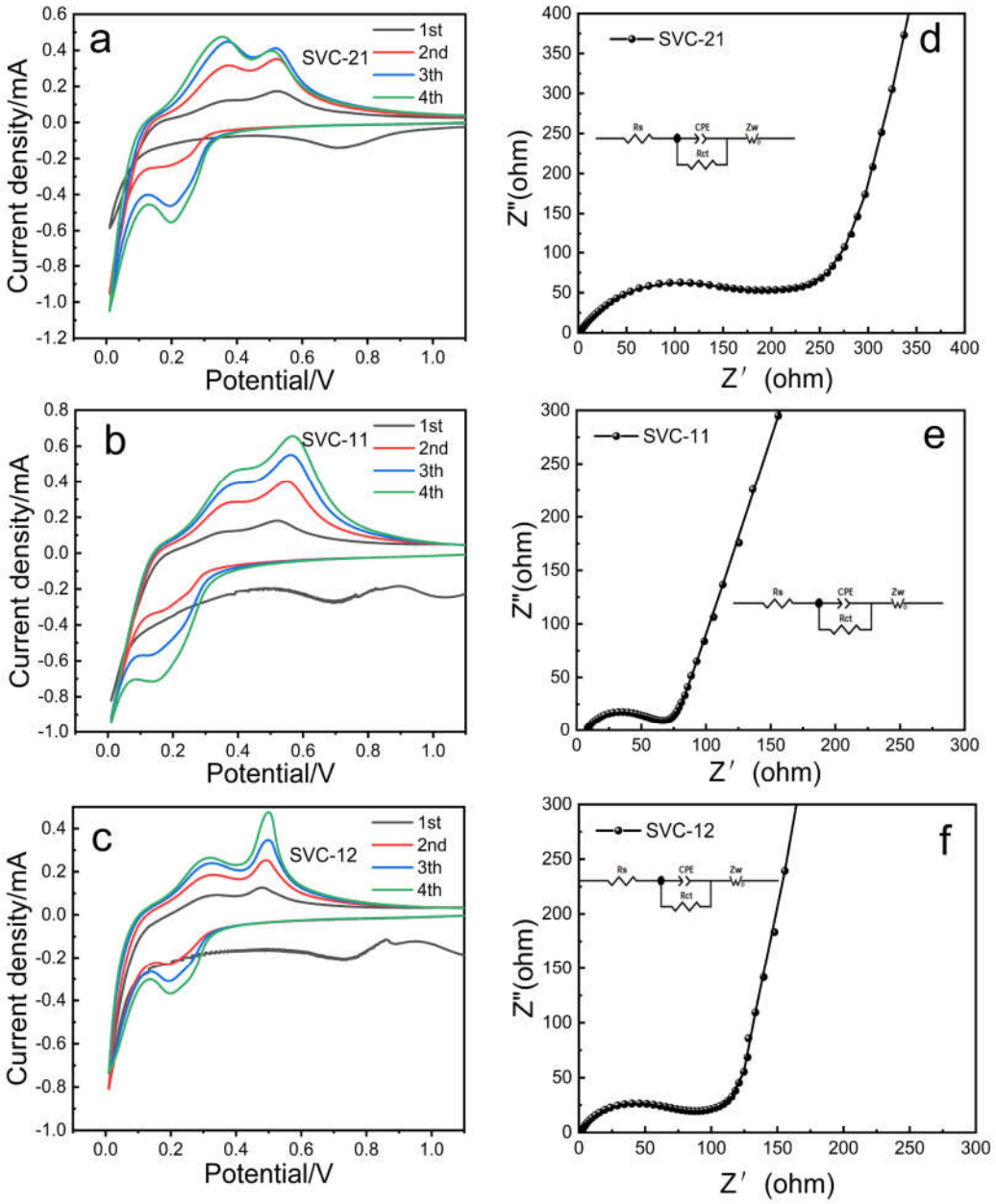

Figure 7. CV curves of SVC-21 (a), SVC-11 (b), and SVC-12 (c), showing the initial four cycles with scanning speed of 0.1 mV s^{-1} at voltage of 0.01-1.1 V; Nyquist plots of the fresh electrodes of SVC-21 (d), SVC-11 (e), and SVC-12 (f).

GCD measurements of Si@void@C electrodes were performed at constant current density of 0.1 A g^{-1} over the voltage range of 0.01–1.2 V for the first three cycles. For comparison, electrode using nanoscale waste Si (WSi) after pretreatment was also prepared and evaluated under the same conditions as described above. As shown in Figure 8a, b, and c, the initial charge/discharge capacities of SVC-21, SVC-11, and SVC-12 are 4097/2718, 1962/1400, and 1609/712 mAh g^{-1}, giving the initial Coulomb efficiency of 66.3%, 71.4%, and 44.3%, respectively. Additionally, the overlapping charge/discharge curves for the second and third cycle further imply the excellent electrochemical

Preprints (www.preprints.org) | NOT PEER-REVIEWED | Posted: 12 May 2023 doi:10.20944/preprints202305.0901.v1

reversibility of Si@void@C, while obvious capacity loss and increasing voltage hysteresis could be observed in charge/discharge curves of WSi (Figure 8d). These results suggest that the amount of "dead lithium" can be effectively reduced, and the volumetric expansion of Si can be suppressed by forming the appropriate proportion of hollow layers and carbon layers.

Figure 9 presents the results of long-term cycling performance of Si@void@C and WSi electrodes at different current densities (0.1, 0.25, 0.5, and 1 A g^{-1}). In the test, the SVC-11 electrode shows the best cycle performance among all the samples, maintaining a discharge capacity of 836 mAh g^{-1} after 100 cycles. SVC-21 and SVC-12 show relatively poor cycle performance with discharge capacity of 345 and 446 mAh g^{-1} after 100 cycles, respectively, but still much higher than that of WSi (33.75 mAh g^{-1}) These results suggest that the amount of "dead lithium" can be effectively reduced, the electronic conductivity can be increased, and the volumetric expansion of silicon can be suppressed by forming the appropriate proportion of hollow layers and carbon layers. The improved cycling performance of Si@void@C should be attributed to its stable yolk-carbon shell structure, which can provide void space to accommodate the huge volume change of Si in the continuous lithiation/delithation processes, thus promoting the transfer of electrons and ensuring the stability of solid electrolyte membranes.

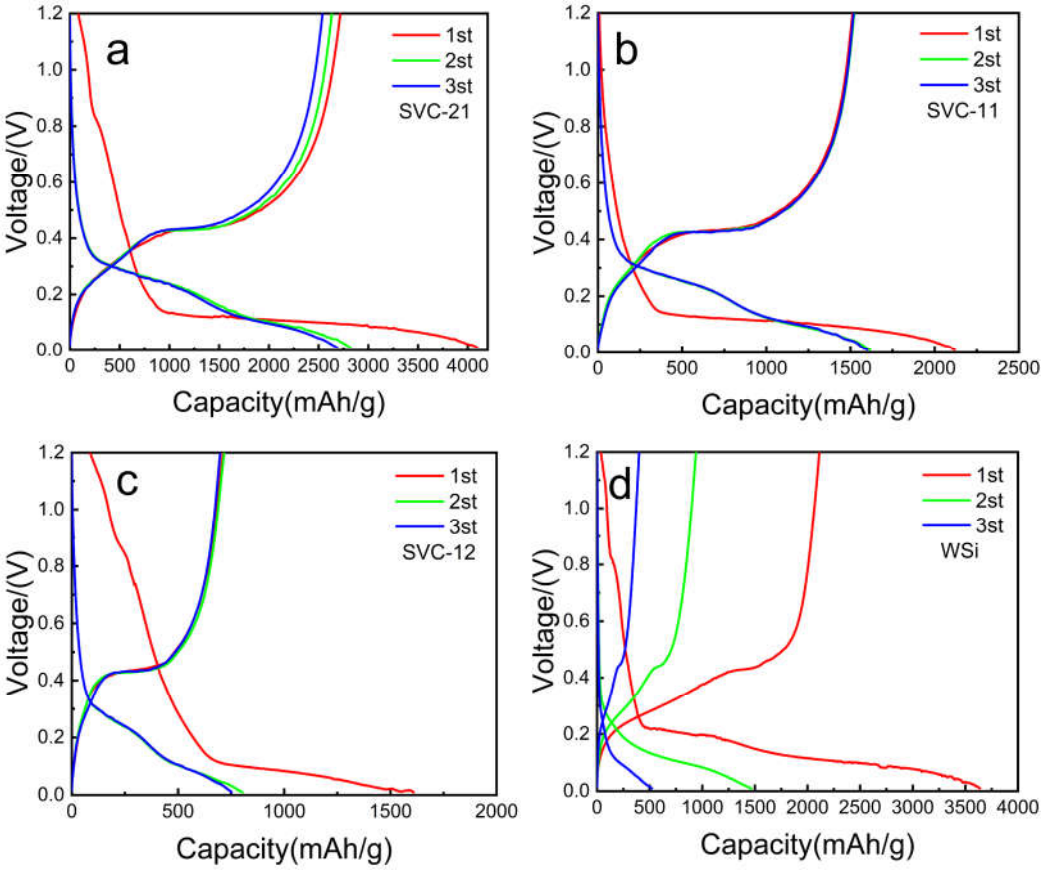

Figure 8. GCD curves at 0.1 A g^{-1} of SVC-21 (a), SVC-11 (b), and SVC-12 (c) and WSi (d).

Preprints (www.preprints.org) | NOT PEER-REVIEWED | Posted: 12 May 2023 doi:10.20944/preprints202305.0901.v1

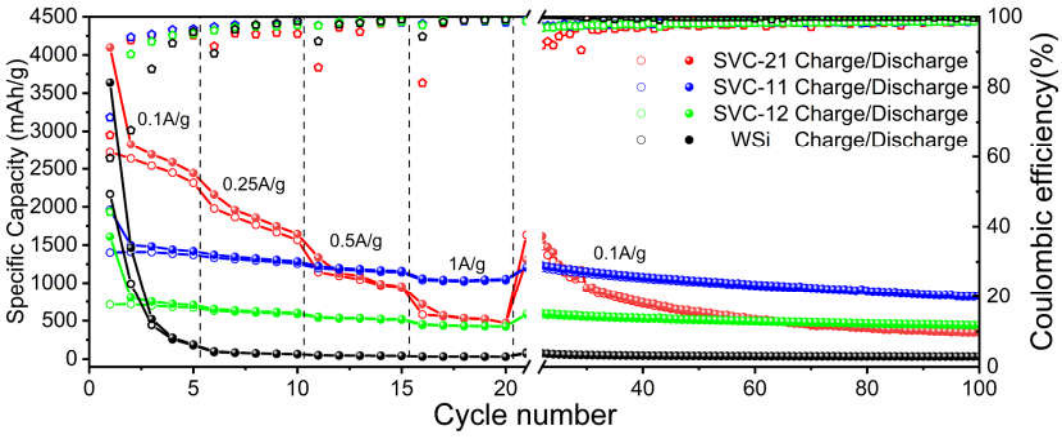

Figure 9. Rate and cycling performance of WSi, SVC-21, SVC-11, and SVC-12.

4. Discussion

The yolk-shell Si@void@C with an intermediate hollow layer is fabricated using KL Si waste as Si source. The intermediate sacrificial layer is generated by metathesis reaction from $AlCl_3$ and ammonia, and the outer carbon shell is generated by hydrothermal process with glucose. Finally, the hollow layer is obtained by etching the intermediate sacrificial layer. Such outer carbon shell could not only decrease the electrical resistance between Si yolks and hollow carbon shells but also effectively protect Si yolks from the formation of Li_2SiF_6 nanolayers on the Si surface. As a result, SVC-11 electrode exhibits remarkably enhanced reversible capacity and cycling stability (~836 mAh g^{-1} after 100 cycles at 0.1 A g^{-1}). The fabrication process involves simple methods and low costs raw materials, produces an anode suitable for practical applications, also contributes to recover Si waste from photovoltaic industry and reduce potentially negative environmental impacts.

Author Contributions: Conceptualization, H.J. and X.L.; formal analysis, H.J. and J.L.; investigation, H.J. and Z.Y.; methodology: Z.L. and X. L.; writing—original draft preparation; H.J. and Z.L.; writing—review and editing, X.L. and K.T.; supervision: X.L. and K.T.; project administration, X.L.; funding acquisition, X.L.; resources, K.T. All authors have read and agreed to the published version of the manuscript.

Funding: This research was supported by Department of Human Resources and Social Security of Jiangsu Province (Jiangsu Postdoctoral Research Funding Program, project No. 2021K180B), Taizhou Science and Technology Bureau (Technology Support Programme, project No. SSF20210131 and TS202202), and Jiangsu University (High-level Scientific Research Foundation for the introduction of talent, project No. 18JDG015).

Institutional Review Board Statement: Not applicable.

Informed Consent Statement: Not applicable.

Data Availability Statement: Data will be made available on request..

Conflicts of Interest: The authors declare no conflflict of interest.

References

1. Xu, Y.; Swaans, E.; Chen, S.; Basak, S.; Harks, P.P.R.; Peng, B.; Zandbergen, H.W.; Borsa, D.M.; Mulder, F.M. A high-performance Li-ion anode from direct deposition of Si nanoparticles. Nano Energy **2017**, 38, 477-485.
2. Zhong, Y.; Wu, P.; Ge, S.; Wu, Y.; Shi, B.; Shao, G.; Gu, C.; Su, Z.; Liu, A. An egg holders-inspired structure design for large-volume-change anodes with long cycle life. J. Alloy Compd. **2020**, 816, 152497.
3. Zhang, C.; Yang, J.; Mi, H.; Li, Y.; Zhang, P.; Zhang, H. A carob-inspired nanoscale design of yolk–shell Si@void@TiO_2-CNF composite as anode material for high-performance lithium-ion batteries. Dalton T. **2019**, 48, 6846-6852.
4. Ji, H.; Luo, T.; Dai, L.; He, Z.; Wang, Q. Topology design of cold plates for pouch battery thermal management considering heat distribution characteristics. Appl. Therm. Eng. **2023**, 224, 119940.

5. Gu, Y.; Jiao, Z.; Wu, M.; Luo, B.; Lei, Y.; Wang, Y.; Wang, L.; Zhang, H. Construction of point-line-plane (0-1-2 dimensional) Fe_2O_3-SnO_2/graphene hybrids as the anodes with excellent lithium storage capability. Nano Res. **2017**, 10, 121-133.
6. Lee, J.I.; Song, G.; Cho, S.; Han, D.Y.; Park, S. Lithium metal interface modification for high-energy batteries: approaches and characterization. Batteries Supercaps **2020**, 3, 828-859.
7. Ji, H.; Li, J.; Li, S.; Cui, Y.; Liu, Z.; Huang, M.; Xu, C.; Li, G.; Zhao, Y.; Li, H. High-Value Utilization of Silicon Cutting Waste and Excrementum Bombycis to Synthesize Silicon–Carbon Composites as Anode Materials for Li-Ion Batteries. Nanomaterials-Basel **2022**, 12, 2875.
8. Ji, H.; Luo, T.; Dai, L.; He, Z.; Wang, Q. Numerical investigation on the polarization and thermal characteristics of $LiFePO_4$-based batteries during charging process. Appl. Therm. Eng. **2022**, 214, 118709.
9. Pan, L.; Wang, H.; Gao, D.; Chen, S.; Tan, L.; Li, L. Facile synthesis of yolk–shell structured Si–C nanocomposites as anodes for lithium-ion batteries. Chem. Commun. **2014**, 50, 5878-5880.
10. Ru, Y.; Evans, D.G.; Zhu, H.; Yang, W. Facile fabrication of yolk–shell structured porous Si–C microspheres as effective anode materials for Li-ion batteries. Rsc Adv. **2014**, 4, 71-75.
11. Sun, Z.; Song, X.; Zhang, P.; Gao, L. Controlled synthesis of yolk–mesoporous shell Si@SiO_2 nanohybrid designed for high performance Li ion battery. Rsc Adv. **2014**, 4, 20814-20820.
12. Sun, Z.; Tao, S.; Song, X.; Zhang, P.; Gao, L. A silicon/double-shelled carbon yolk-like nanostructure as high-performance anode materials for lithium-ion battery. J. Electrochem. Soc. **2015**, 162, A1530.
13. Reverchon, E.; Adami, R. Nanomaterials and supercritical fluids. J. Supercrit. Fluid. **2006**, 37, 1-22.
14. Wang, T.; Lin, Y.; Tai, C.; Sivakumar, R.; Rai, D.; Lan, C. A novel approach for recycling of kerf loss silicon from cutting slurry waste for solar cell applications. J. Cryst. Growth **2008**, 310, 3403-3406.
15. Le Donne, A.; Acciarri, M.; Narducci, D.; Marchionna, S.; Binetti, S. Encapsulating Eu^{3+} complex doped layers to improve Si-based solar cell efficiency. Prog. Photovoltaics **2009**, 17, 519-525.
16. Drouiche, N.; Cuellar, P.; Kerkar, F.; Medjahed, S.; Boutouchent-Guerfi, N.; Hamou, M.O. Recovery of solar grade silicon from kerf loss slurry waste. Renew. Sust. Energ. Rev. **2014**, 32, 936-943.
17. Xiang, K.; Wang, X.; Chen, M.; Shen, Y.; Shu, H.; Yang, X. Industrial waste silica preparation of silicon carbide composites and their applications in lithium-ion battery anode. J. Alloy Compd. **2017**, 695, 100-105.
18. Liu, N.; Wu, H.; McDowell, M.T.; Yao, Y.; Wang, C.; Cui, Y. A yolk-shell design for stabilized and scalable Li-ion battery alloy anodes. Nano Lett. **2012**, 12, 3315-3321.
19. Li, H.; Wang, J.; Wu, X.; Sun, H.; Yang, F.; Wang, K.; Zhang, L.; Fan, C.; Zhang, J. A novel approach to prepare Si/C nanocomposites with yolk–shell structures for lithium ion batteries. RSC Adv. **2014**, 4, 36218-36225.
20. Zhang, L.; Rajagopalan, R.; Guo, H.; Hu, X.; Dou, S.; Liu, H. A Green and Facile way to prepare Granadilla-like silicon-based anode materials for Li-ion batteries. Adv. Funct. Mater. **2016**, 26, 440-446.
21. Yang, T.; Gao, Y.; Tang, Y.; Zhang, Y.; Li, X.; Liu, L. Porous silicon from industrial waste engineered for superior stability lithium-ion battery anodes. J. Nanopart. Res. **2021**, 23, 1-11.
22. Liu, W.; Liu, J.; Zhu, M.; Wang, W.; Wang, L.; Xie, S.; Wang, L.; Yang, X.; He, X.; Sun, Y. Recycling of lignin and Si waste for advanced Si/C battery anodes. ACS Appl. Mater. Interfaces **2020**, 12, 57055-57063.
23. Zhang, J.; Li, S.; Xi, F.; Wan, X.; Ding, Z.; Chen, Z.; Ma, W.; Deng, R. Si@SiO_x/Ag composite anodes with high initial coulombic efficiency derive from recyclable silicon cutting waste. Chem. Eng. J. **2022**, 447, 137563.
24. Sevilla, M.; Fuertes, A.B. The production of carbon materials by hydrothermal carbonization of cellulose. Carbon **2009**, 47, 2281-2289.
25. Yang, H.; Wang, G.; Ding, N.; Yin, C.; Chen, Y. Size-controllable synthesis of carbon spheres with assistance of metal ions. Synthetic Met. **2016**, 214, 1-4.
26. Lu, Y.; Chang, P.; Wang, L.; Nzabahimana, J.; Hu, X. Yolk-shell Si/SiO_x@Void@C composites as anode materials for lithium-ion batteries. Funct. Mater. Lett. **2019**, 12, 1850094.
27. Wu, Y.; Han, T.; Zhou, T.; Qiao, X.; Chen, X.; Zhou, P.; Liu, J. A novel silicon nanoparticles-infilled capsule prepared by an oil-in-water emulsion strategy for high-performance Li-ion battery anodes. Nanotechnology **2020**, 31, 335403.
28. Mi, H.; Yang, X.; Li, Y.; Zhang, P.; Sun, L. A self-sacrifice template strategy to fabricate yolk-shell structured silicon@void@ carbon composites for high-performance lithium-ion batteries. Chem. Eng. J. **2018**, 351, 103-109.
29. Shao, T.; Liu, J.; Gan, L.; Gong, Z.; Long, M. Yolk-shell Si@void@C composite with Chito-oligosaccharide as a C–N precursor for high capacity anode in lithium-ion batteries. J. Phys. Chem. Solids **2021**, 152, 109965.
30. Zhou, Z.; Pan, L.; Liu, Y.; Zhu, X.; Xie, X. From sand to fast and stable silicon anode: synthesis of hollow Si@void@C yolk–shell microspheres by aluminothermic reduction for lithium storage. Chinese Chem. Lett. **2019**, 30, 610-617.
31. Yoon, D.; Kim, D.H.; Chung, K.Y.; Chang, W.; Kim, S.M.; Kim, J. Hydrogen-enriched porous carbon nanosheets with high sodium storage capacity. Carbon **2016**, 98, 213-220.

 doi:10.20944/preprints202305.0901.v1

32. Zeng, S.; Chen, X.; Xu, R.; Wu, X.; Feng, Y.; Zhang, H.; Peng, S.; Yu, Y. Boosting the potassium storage performance of carbon anode via integration of adsorption-intercalation hybrid mechanisms. Nano Energy **2020**, 73, 104807.
33. Ji, H.; Chen, Q.; Hua, K.; Ma, Q.; Wang, R.; Zhang, L.; Zhang, C. Si nanoparticles embedded in porous N-doped carbon fibers as a binder-free and flexible anode for high-performance lithium-ion batteries. J. Alloy Compd. **2023**, 936, 168256.
34. Feng, Y.; Liu, L.; Liu, X.; Teng, Y.; Li, Y.; Guo, Y.; Zhu, Y.; Wang, X.; Chao, Y. Enabling the ability of Li storage at high rate as anodes by utilizing natural rice husks-based hierarchically porous SiO_2/N-doped carbon composites. Electrochim. Acta **2020**, 359, 136933.
35. Domi, Y.; Usui, H.; Shimizu, M.; Kakimoto, Y.; Sakaguchi, H. Effect of phosphorus-doping on electrochemical performance of silicon negative electrodes in lithium-ion batteries. ACS appl. Mater. Interfaces **2016**, 8, 7125-7132.
36. Liu, M.; Fan, H.; Zhuo, O.; Chen, J.; Hu, Z. A general strategy to construct yolk-shelled metal oxides inside carbon nanocages for high-stable lithium-ion battery anodes. Nano Energy **2019**, 68, 104368.
37. Zhang, Y.C.; You, Y.; Xin, S.; Yin, Y.X.; Guo, Y.G. Rice Husk-Derived Hierarchical Silicon/Nitrogen-Doped Carbon/Carbon Nanotube Spheres as Low-Cost and High-Capacity Anodes for Lithium-Ion Batteries. Nano Energy **2016**, 25, 120-127.
38. Ji, H.; Tao, L.; Hu, B.; Xu, J.; Ding, J. Enhanced rate and low-temperature performance of $LiFePO_4$ cathode with 2D Ti_3C_2 MXene as conductive network. Electroanal Chem. **2023**, 928, 117047.